Physicochem. Probl. Miner. Process., 61(4), 2025, 208769

http://www.journalssystem.com/ppmp

Physicochemical Problems of Mineral Processing

ISSN 1643-1049

Multi factor analysis of the vertical roller mill separator based on BP neural network - response surface joint modeling

Zhengyang Bi [1], Lei Zheng [1], Tianshuo Li [1], Baolin Zhang [2], Hongchao Ji [1], Zibo Zhao [1]

[1] College of Mechanical Engineering, North China University of Science and Technology, Tangshan, Hebei, China, 063000

[2] Tangshan Jidong Equipment Engineering Co., Ltd, Tangshan, Hebei, China, 063000

Corresponding author. zhenglei1@163.com (Lei Zheng)

Abstract: This study investigates multi-factor dynamics in vertical roller mill separator using a BP neural network-Response Surface Methodology (BP-RSM) framework. Computational Fluid Dynamics (CFD) with a Dense Discrete Phase Model (DDPM) simulates particle motion, generating 60 datasets. The BP neural network achieves an integrated determination coefficient of 97.05% on these data, expanding to 12,150 virtual experiments. The relationships of the data generated by the BP neural network were expressed through RSM, realizing an explicit and visual representation of multiple factors (with an integrated determination coefficient of 99.76% and a predicted determination coefficient of 99.75%), therefor the validation determination coefficient of BP-RSM joint fitting is 96.82%. BP-RSM surpasses traditional RSM in generalization and interpretability. The results indicate that the air injection velocity (v_g), rotor rotation speed (ω), and rotor diameter ratio (d/d_0) are significant factors influencing the separation size (d_c). The variation in the rotor diameter ratio (d/d_0) can modulate the intensity of vortices generated between moving blades, which significantly influences the adaptation to fluctuations in air injection velocity (v_g). In the target particle size range of 40-60 μm, the rotor diameter ratio (d/d_0) of separator is between 1.2 and 1.4. This configuration can enhance the adaptability of the equipment's air injection velocity (v_g) by a factor of 2-3 times. This framework effectively addresses the challenges associated with multifactor coupled modeling and the explicit representation of high-dimensional nonlinear relationships. It offers a solution for the multi-objective optimization of separators that is easy to operate, while ensuring both predictive accuracy and physical interpretability.

Keywords: vertical roller mill separator, CFD-DDPM simulation, multifactor analysis, the BP neural network, response surface methodology (RSM)

1. Introductory

As a type of high-efficiency and energy-saving equipment, the vertical roller mill integrates the functions of grinding, drying, and classifying. Its widespread application in powder processing within the cement and mining industries can be attributed to its energy-saving advantages when compared to traditional ball mills (Fatahi et al., 2002; Hu et al., 2025; Wang et al., 2009). As a fundamental component of the vertical roller mill system, the separator facilitates particle separation by establishing a dynamic equilibrium between the centrifugal force field produced by the high-speed rotation of the rotor and the traction field generated by airflow. The accuracy of this separation has a direct impact on both product size distribution and overall system energy consumption (Li et al., 2016). Studies have demonstrated that the precise control of the separation size (d_c) significantly influences the properties of cement. Key performance indicators include setting time and exothermic hydration, among others. Studies such as Esmaeilpour et al. (2024) and Pareek et al. (2021) confirmed through Computational Fluid Dynamics (CFD) simulations that optimizing the separation size (d_c) can reduce the separator's energy consumption by 14.63% and increase its capacity from 203 t/h to 214 t/h, representing a growth of 5.4%. In terms of research methodology, the vertical roller mill is classified as large-scale equipment. The synergistic analysis of its structural and operational parameters often employs Computational Fluid

DOI: 10.37190/ppmp/208769

Dynamics (CFD) methods. This approach not only significantly reduces experimental costs but also enables a detailed characterization of the internal flow field within the vertical roller mill (Ismail et al., 2022; Hu et al., 2025; Li et al., 2024).

The current research on the separation mechanism of separators primarily focuses on single-factor and two-factor analyses, with a limited number of studies utilizing approximate models for three-factor coupling to optimize solutions. For instance, Geng et al. (2021) quantitatively elucidated the independent influence of system air volume and separator speed through mathematical modeling. Their findings indicated that a 10% increase in air volume could lead to an increase in cut particle size by 8-12 μm, where as a rise of 100 rpm in rotational speed could reduce the fineness of the finished product (measured as residue on an 80 μm sieve) by approximately 3-5%. Esmaeilpour et al. (2024) conducted a univariate analysis focusing on parameters such as feeding percentage and blade shape, highlighting that there remains an optimization potential of 15-20% for the current parameter regulation. Xu et al. (2000) conducted a two-factor test and discovered that, when the blade pitch is held constant, there exists a nonlinear coupling effect between the air volume and the feed concentration. Furthermore, the maximum particle size of fine particles exhibits a complex trend characterized by an initial increase, followed by a decrease, and then another increase. Huang et al. (2023) proposed a numerical calculation method for the coupled particle-fluid system within a large vertical mill, based on CFD-DPM theory and a multi-objective optimization approach. They employed the Kriging surrogate model to conduct a three-factor analysis involving inlet air velocity, powder separator speed, and outlet temperature. Subsequently, the NSGA-II algorithm was utilized to update the agent model and identify the optimal solution, resulting in an increase in vertical mill output by 5.34%.

As a systematic project, the parameters of the separator are interrelated, and the mechanisms underlying performance changes involve the synergistic effects of multiple factors. This complexity reflects a high degree of intricacy, while the interaction among various parameters may further exacerbate these nonlinear effects. The flow field simulation conducted by Sun et al. (2012) indicates that the vortex flow within the separator interferes with the balance of traction and centrifugal forces. It is challenging to comprehensively elucidate its intrinsic principles through single-factor or two-factor analyses alone. Therefore, it is essential to investigate the effects of multiple factors in a coupled manner. However, as the number of factors increases and the experimental combinations expand exponentially, it becomes essential to implement more targeted data processing strategies. This approach is crucial for uncovering high-dimensional nonlinear relationships in engineering applications and achieving effective representations.

The neural network methodology plays a crucial role in the detection of equipment faults and the prediction of performance under multifactorial conditions. Fatahi et al. (2025) employed XGBoost to achieve a high level of accuracy in predicting working pressure. Additionally, they utilized SHAP analysis to elucidate the model's decisions and quantify the contribution of each parameter to the working pressure. The S-type nonlinear interaction relationship between differential pressure and feed rate was established through multi-factor coupling, leading to the optimization of the matching process between roll pressure and feed rate. Based on this, the "Consciousness Lab" framework integrates data-driven approaches with physical mechanisms to deliver interpretable real-time decision support for the optimization of industrial processes. However, Dobson et al. (2023) found that the black-box nature of neural networks poses challenges in obtaining a mathematical representation of the model for visualization purposes. In this context, Response Surface Methodology (RSM) can effectively and intuitively provide a representation suitable for multi-factor problems. Combined with hydrodynamic simulation cases, a visual representation of the multifactorial problem can be achieved, facilitating a more in-depth and intuitive exploration of its intrinsic principles. For instance, Taghinezhad et al. (2023) developed an optimization strategy that integrates Computational Fluid Dynamics (CFD) with Response Surface Methodology (RSM) to determine the optimal throat wind speed and constriction ratio. This approach aims to enhance the throat wind speed and output power of conduit-type wind turbines, ultimately reducing both design costs and time. However, the accuracy of its predictions is significantly influenced by both the volume of data available and the mathematical representation of the internal mechanisms pertaining to the research subject (Wang et al., 2022). Both approaches possess distinct advantages and illustrate the potential for complementing one another's strengths while

reinforcing their respective merits.

To this end, the present study seeks to leverage the strengths of neural networks in addressing complex nonlinear problems, while integrating the explicit expression capabilities of Response Surface Methodology (RSM). This approach aims to achieve a more accurate representation of flow field relationships with a reduced amount of sample data. In-depth discussion of the five key factors influencing the separator performance in vertical roller mills: particle injection mass (m_p), particle injection velocity (v_p), rotor rotation speed (ω), air injection velocity (v_g), and rotor diameter ratio (d/d_0). This analysis aims to identify the core factors affecting the separation law of separation size and to develop an optimization program. This method not only provides a theoretical foundation and analytical solution for the design of operating parameters in separators, but also introduces innovative ideas and directions for future research on more complex influencing factors and conditions.

2. Separator structure and force principle

2.1. Separator structure and powder selection process

The separation region of the separator is comprised of a gravitational zone and a centrifugal zone (Altun et al., 2017), as illustrated in Fig. 1. In the working process of the vertical roller mill, as illustrated in Fig. 1(a), high-speed airflow from the nozzle ring carries material particles upward during grinding. In this ascending phase, larger particles are influenced by gravity and fall back onto the grinding disk to continue the grinding process (Huang et al., 2024). The smaller-sized material particles enter the centrifugal separation zone following gravity grading. At this stage, the material particles, influenced by the airflow and static blades, are directed into the annular region formed by both the static and rotor blades. In this region, the trailing force produced by the airflow interacts with the centrifugal force, resulting in the formation of a vortex, as illustrated in Fig. 1(b). The material particles within the separator undergo secondary separation as a result of the combined effects of trailing force and centrifugal force.

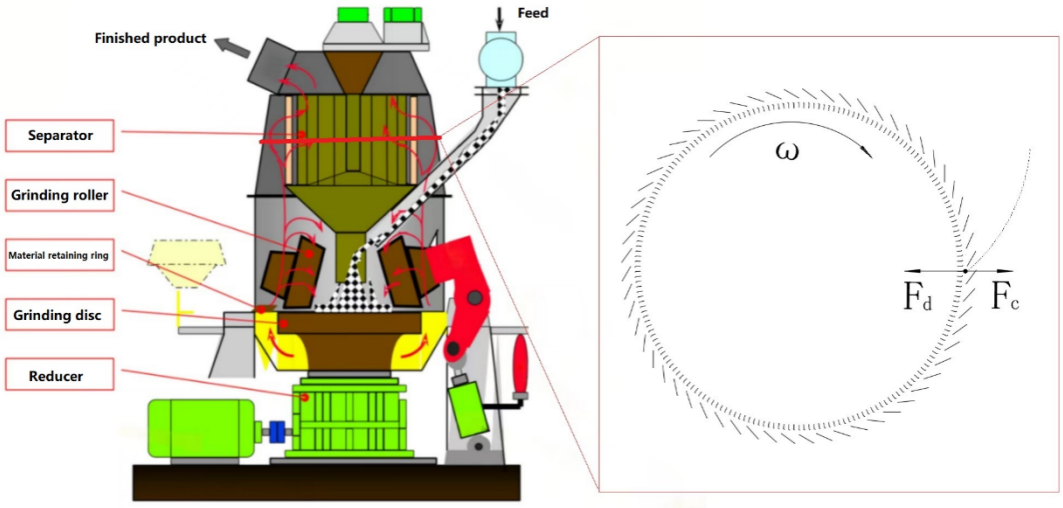

(a) Working process diagram of vertical roller mill. (b) Annular area formed by static and rotor blades.

Fig. 1. Schematic representation of the separator in a vertical roller mill

2.2. Forces acting on particles in separation processes

Material particles entering the separator are subjected to both trailing force and centrifugal force. If the trailing force exceeds the centrifugal force, the particles will be carried out of the separator by the airflow. Conversely, if the centrifugal force prevails, the particles will enter the fallback channel and ultimately settle into the coarse powder collection port.

The centrifugal and trailing forces acting on the particles within the separator are presented in Eq. 1 and Eq. 2, respectively:

$$F_c = \frac{\pi}{6} d_p^3 \rho_p \omega_p{}^2 r \tag{1}$$

$$F_d = K \rho_g d_p^2 (v_{gt} - v_{pt})^2 \tag{2}$$

where: the trailing force is denoted as F_d, the centrifugal force is represented by F_c, and the particle size of the material entering the separator is indicated as d_p. The particle density and air density are referred to as ρ_p and ρ_g, respectively. The angular velocity of the particles is expressed as the equation ($\omega_p = v_{pr}/r$), while the radial flow velocity of air is designated as v_{gt}. The radial flow velocity of particles is represented by v_{pt}, with the circumferential flow velocities for air and particles being denoted as v_{gr} and v_{pr}, respectively. Additionally, r signifies the particle rotational radius, and *K* represents the drag coefficient.

It can be observed from Eq. 1 and Eq. 2 that the centrifugal force is proportional to the cube of the particle diameter, whereas the trailing force is proportional to the square of the particle diameter. When the centripetal force (F_c) equals the drag force (F_d), the material particles will maintain a continuous rotational motion along a track with radius r. However, when the particle size increases such that F_c exceeds F_d, the resultant force acting on the material particles is directed opposite to the center of rotation. In this scenario, the particles will experience centrifugal motion, moving tangentially and colliding with static blades, resulting in a loss of momentum. Subsequently, they will descend onto the grinding disc for secondary grinding.

When the particle size is small, and the condition ($F_c < F_d$) holds, the resultant force acting on the particles directs towards the center of rotation. Consequently, these particles will undergo centripetal motion, moving inward toward this center. This principle facilitates the selection of fine particles that conform to the specified material particle size standards, thereby achieving effective particle separation.

When the forces F_c and F_d are equal, the separation size (d_c) can be determined as follows:

$$\frac{\pi}{6} d_c^3 \rho_p v_{pr}^2 / r = K \rho_g d_c^2 (v_{gt} - v_{pt})^2 \tag{3}$$

$$d_c = \frac{6K\rho_g}{\pi \rho_p} \cdot \frac{(v_{gt} - v_{pt})^2 r}{v_{pr}^2} \tag{4}$$

Under multi-particle conditions, it is essential to incorporate the momentum exchange between the particle and air phases into the interphase force for proper balance. Specifically, this entails acknowledging that momentum transfer occurs between the particles and the air. The interphase force is primarily influenced by the trailing force equation. The traction force is represented in the multiphase flow volume balance Eq. 5 (Adnan et al., 2021) as follows:

$$F_d = \beta (v_g - v_p) \tag{5}$$

where, in accordance with the Wen-Yu traction model (Gidaspow et al., 1992), β represents the traction coefficient and is defined as follows:

$$\beta = \frac{3}{4} C_D \frac{\varepsilon_p \varepsilon_g \rho_g \left| \vec{v}_p - \vec{v}_g \right|}{d_p} \varepsilon_g^{-2.65}, \varepsilon_g \geq 0.8 \tag{6}$$

where: $C_D = \frac{24}{\varepsilon_g R_e} \left[1 + 0.15 \left(\varepsilon_g R_e \right)^{0.687} \right], R_e \leq 1000$

$C_D = 0.44, R_e > 1000$

where: β represents the drag coefficient as defined by the Wen-Yu drag model. The variables ε_g and ε_p denote the volume fractions of the air and solid phases, respectively. Additionally, ρ_g indicates the density of the air phase, while $\vec{v}_p$ and $\vec{v}_g$ are the velocity vectors corresponding to the solid and air phases, respectively. The term d_p refers to the diameter of a particle, and R_e signifies the Reynolds number. C_D is defined as the effective drag coefficient for a particle.

2.3. Objectives and programs for parametric analysis

From Eq. 4 and Eq. 6, it is evident that the separation size (d_c) during the particle movement process in a vertical roller mill is primarily influenced by several factors, including the particle injection mass (m_p), particle injection velocity (v_p), rotor rotation speed (ω), air injection velocity (v_g), and rotor diameter

ratio (d/d_0). The response variable of this study is the separation size (d_c). Taking into account the vortex strength between blades, particle concentration, particle motion velocity, and air motion velocity as influenced by equipment structure and operating parameters—considered here as passive and indirect analysis targets (Sun et al., 2012)—we establish fixed parameters including air viscosity, particle density, air density, flow field structure, and collision coefficient. Subsequently, we conduct fluid simulations to perform multi-factor analyses and mechanism investigations. This resulted in the establishment of the analytical framework illustrated in Fig. 2.

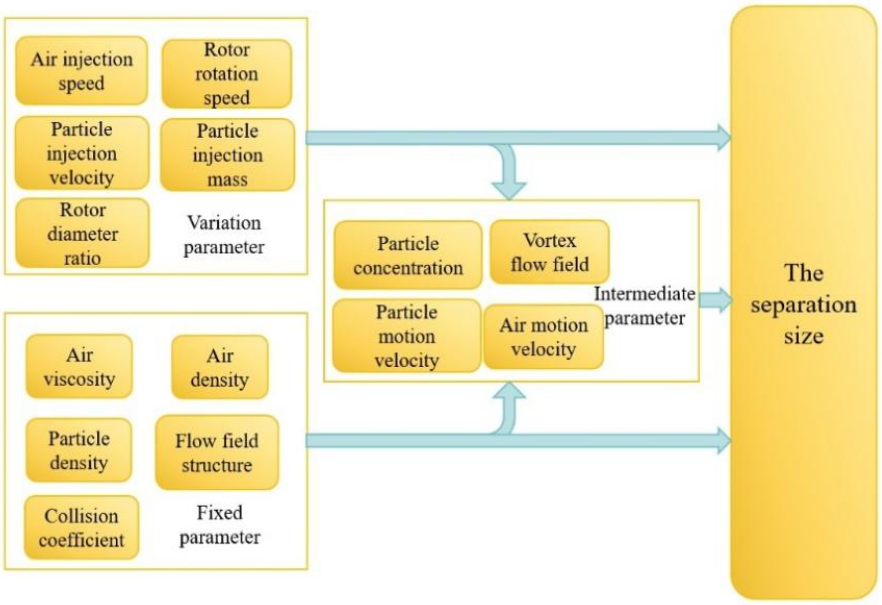

Fig. 2. Critical factors influencing separation

3. Simulation experiment and data analysis program

3.1. Simulation model

To derive the flow field characteristics, the vertical roller mill body and the separator blade region are modeled and simulated separately. The vertical roller mill body is modeled in three dimensions, with an emphasis on understanding the overall flow field and air injection velocity (v_g) of the separator. In contrast, the separator component focuses on examining the motion state of particles in proximity to the rotor blades. Additionally, two-dimensional planes within the regions of both static and moving blades are extracted to conduct simulation analyses using a more refined mesh.

To enhance computational efficiency, the vertical roller mill body employs a 1/3 periodic boundary to establish the flow field structure model. Subsequently, a hexahedral mesh is utilized, as illustrated in Fig. 3(a). The maximum cell size is set at 0.06 m, resulting in a total of 540,000 meshes. The maximum vertical-to-horizontal ratio of the mesh is 18.9, and the mass fraction of the mesh that is less than 0.4145 accounts for only 0.1%.

The rotor region is dedicated to characterizing the separation behavior of particles under conditions influenced by trailing force and centrifugal force, while disregarding the effects of gravity. This analysis focuses on intercepting the structure of the planar annular region, as illustrated in Fig. 3(b) and Fig. 3(c). A periodic boundary condition with a ratio of 1/10 was implemented, and a quadrilateral-dominated grid model was utilized, as illustrated in Fig. 3(d). The grid comprised a total of 34,962 elements, featuring a grid size of 0.005 m and an aspect ratio that reached a maximum value of 3.81.

3.2. Numerical simulation of air-solid two-phase flow in a vertical roller mill for cement production

According to the operating parameters of the vertical roller mill, the mass concentration (C) of particles in the air stream typically 0.9 Nm³/kg (standard cubic meter per kilogram of material). The density ρ_p of cement particles is approximately 2800 kg/m³. Based on the equation ($C = \varepsilon_p \rho_p$), the particle volume

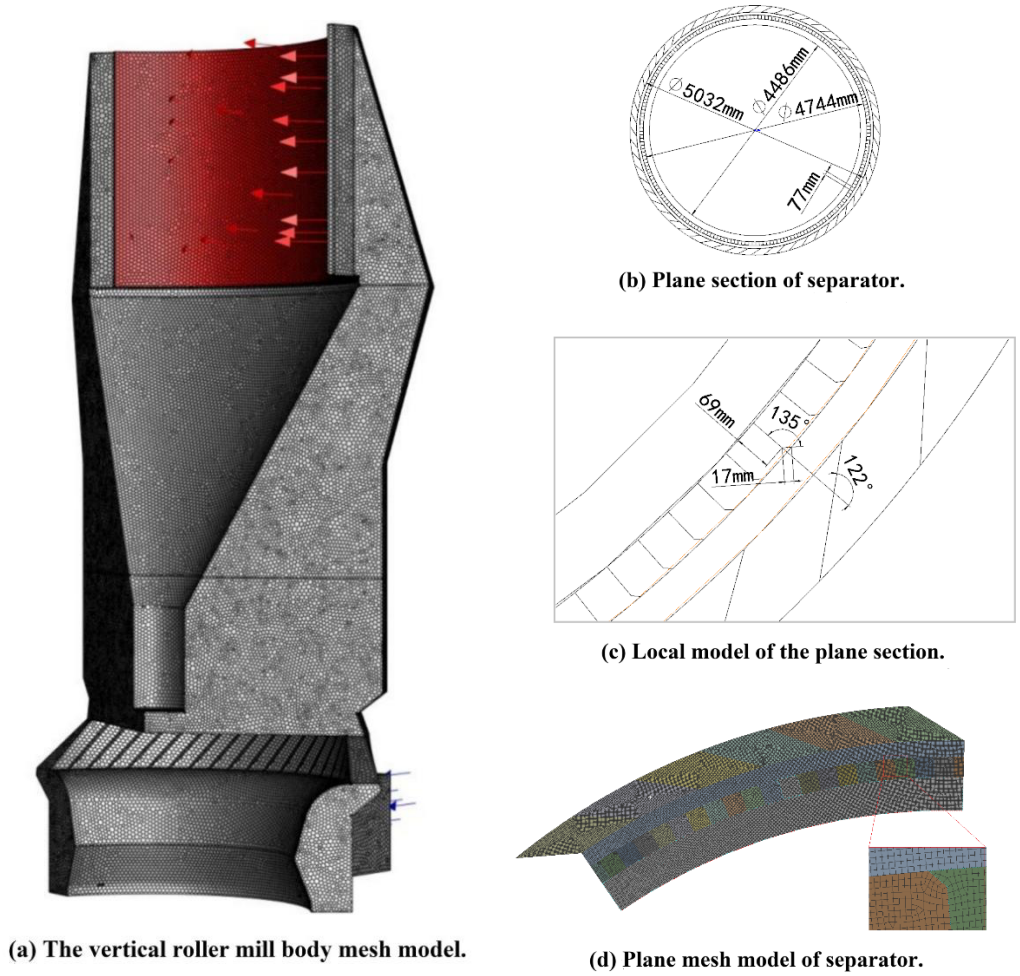

(a) The vertical roller mill body mesh model.

(b) Plane section of separator.

(c) Local model of the plane section.

(d) Plane mesh model of separator.

Fig. 3. Vertical roller mill body structure and mesh modeling

fraction ε_p in the air-solid mixed flow is estimated to be around 0.03% (Huang et al., 2023). Although the volume fraction is low and theoretically exerts a negligible influence on air flow in the primary region, it is essential to consider the substantial increase in mixing density resulting from particle loading within the momentum exchange model. This particle state is encompassed within the framework of the bidirectionally coupled Discrete Phase Model (DPM) (Bagherzadeh et al., 2024). However, substantial localized particle aggregation was observed in the high-velocity gradient region between the moving and static blades. This area exhibited a complex flow field that approached the critical zone for particle separation. To more effectively illustrate the particle agglomeration phenomenon in this region and to improve the validity of the simulation, the Dense Discrete Phase Model (DDPM) (Xu et al., 2024) was employed. The model enhances the applicability of the traditional DPM framework and is better suited for representing particulate flow fields by incorporating particle-specific forces and an improved interphase coupling mechanism.

Anisotropic reflection coefficients were employed for the wall boundary conditions to accurately characterize the behavior of particle-wall collisions. Referring to the experimental measurements conducted by Wang et al. (2024), the normal and tangential reflection coefficients are set at 0.1 and 0.5, respectively. This specific combination of parameters effectively captures the velocity differences observed in various directions when material particles collide with both moving and static blades.

To enhance the representation of the vortex flow field between moving blades and to improve computational efficiency, the RNG k-ε turbulence model has been employed.

To investigate the differences in emissions associated with various particle sizes, the range of particle diameters (V) was established as [10, 500], rounding to the nearest ten for a set of fifty particles. The particles possess a density of 2800 kg/m³ and are injected in the face-normal direction, exhibiting a uniform distribution of diameters. The five key variables, namely particle diameter (V), particle injection

mass (m_p), particle injection velocity (v_p), rotor rotation speed (ω), air injection velocity (v_g), and rotor diameter ratio (d/d_0), are collectively referred to as core simulation parameters for the convenience of subsequent analysis and description. Its scope is shown in Table 1. In the simulation, to ensure a proportional relationship between the static and moving blades of the separator rotor, as well as the positioning of the moving blades, we set the rotor diameter ratio as d/d_0, where d_0 (5032 mm) represents the diameter of the current equipment prototype separator rotor.

Table 1. Simulation parameter setting range

	V (μm)	m_p (kg/s)	v_p (m/s)	ω (rad/s)	v_g (m/s)	d/d_0
Range	[10, 500]	[15, 30]	[1.2, 15]	[4, 20]	[3, 15]	[0.5, 1.5]

3.3. Refinement of evaluation program

To quantify the characteristics of particle separation, this study introduces the concept of escape rate. This is defined as the ratio of net outflow to net injection of particles of a specific size during a steady-state flow period. Numerical simulation results indicate that the flow state of the system tends to stabilize at 0.2 seconds. Consequently, the time interval from 0.6 to 1.6 seconds is selected for data statistics in order to mitigate transient interference. The escape rate α_i is determined using the following equation:

$$\alpha_i = \left(1 - \frac{n'_{i,1.2} - n'_{i,0.6}}{n_{i,1.2} - n_{i,0.6}}\right) \times 100\% \tag{7}$$

where: $n'_{i,1.2}$ denotes the outflow at 1.2 seconds for the ith particle size; $n'_{i,0.6}$ indicates the outflow at 0.6 seconds for the ith particle size; $n_{i,1.2}$ represents the injected amount at 1.2 seconds for the ith particle size; and $n_{i,0.6}$ refers to the injected amount at 0.6 seconds for the ith particle size. In response to the subsequent investigation into the necessity of a separation size under multifactorial conditions, an escape rate exceeding 80% was established as indicative of effective separation. The particle size corresponding to this threshold is defined as the separation size (d_c).

The simulation was conducted in accordance with the methodology outlined in Table 1. The escape rate was calculated based on the framework presented in Table 2. Subsequently, the separation size (d_c) was determined using the escape rate, and the results of the simulation experiments are summarized in Table 2.

Table 2. Data sheet for simulation experiment

Number	m_p (kg/s)	v_p (m/s)	ω (rad/s)	v_g (m/s)	d/d_0	d_c (μm)
1	25	1.8	12	3	1.5	20
2	25	3	12	3	1.5	20
3	20	2.4	12	3	0.5	40
4	20	2.4	12	3	1	40
5	20	2.4	16	6	1	40
6	20	4.8	16	6	1	40
7	25	6	16	6	0.75	40
8	30	4.8	16	6	1	40
9	20	1.2	12	3	0.5	50
10	15	3.6	16	6	0.75	50
11	25	3.6	16	6	0.75	50
12	25	9	12	9	1.5	60
13	25	5.4	12	9	1.5	60
14	15	3.6	9	6	1.5	60
15	15	8	13	10	1.5	60
16	20	4.8	16	12	1	70

17	20	3.6	20	9	0.5	70
18	30	9.6	16	12	1	70
19	30	7.2	12	9	1	70
20	20	9.6	16	12	1	80
21	15	3.6	10	9	1.5	80
22	25	7	8	7	0.75	80
23	30	3	8	5	1	80
24	25	7.2	16	12	0.75	90
25	25	12	16	12	0.75	90
26	15	5	6	5	1.5	90
27	20	2.4	8	6	1	100
28	20	4.8	8	6	1	100
29	30	4.8	8	6	1	100
30	20	2.4	7	4	0.75	100
31	25	5	8	5	0.75	100
32	25	7.2	15	12	1.5	100
33	25	9	12	15	1.5	110
34	25	15	12	15	1.5	110
35	30	4.8	9	8	1	110
36	15	3.6	8	6	0.75	120
37	25	3.6	8	6	0.75	120
38	25	6	8	6	0.75	120
39	15	1.2	6	3	0.5	120
40	25	5.4	11	9	0.75	120
41	20	4.8	10	6	0.5	130
42	20	3.6	12	9	0.5	140
43	20	7.2	12	9	0.5	140
44	20	11	14	11	0.5	140
45	20	7.2	20	9	0.5	140
46	20	6	18	15	0.5	150
47	20	8	11	10	0.5	190
48	20	3.6	7	6	0.5	190
49	20	4.8	8	12	1	200
50	20	9.6	8	12	1	200
51	15	7.2	8	12	0.75	210
52	30	9.6	8	12	1	210
53	25	9	4	9	1.5	240
54	25	3.6	4	9	1.5	240
55	20	6	12	15	0.5	250
56	20	12	12	15	0.5	250
57	25	12	8	12	0.75	250
58	25	5.4	4	9	1.5	250
59	25	7.2	8	12	0.75	270
60	30	9.6	8	12	0.5	350

3.4. Data analysis program

3.4.1. Application of BP neural network for data fitting

In order to establish the nonlinear coupling relationship among the core simulation parameters and the separation size (d_c), a multilayer feed-forward backpropagation (BP) neural network was employed to

predict the separation size (d_c) under the synergistic influence of multiple factors. The model architecture is illustrated in Fig. 4 and comprises the following components: an input layer that receives five-dimensional feature vectors corresponding to the aforementioned five categories of key influencing factors; a hidden layer consisting of five neuron nodes, utilizing a sigmoid activation function ($\sigma(x) = 1/(1+e^{-x})$) to capture nonlinear features and ensure output smoothness; and an output layer that employs a linear activation function to classify the separation size (d_c) as a single response variable. The dataset comprises 60 sets of numerical simulation results, which are randomly partitioned into a training set (42 sets), a validation set (9 sets), and a test set (9 sets) in the ratio of 70%:15%:15%. The network is trained utilizing the Levenberg-Marquardt optimization algorithm, with the mean square error (MSE) serving as the loss function.

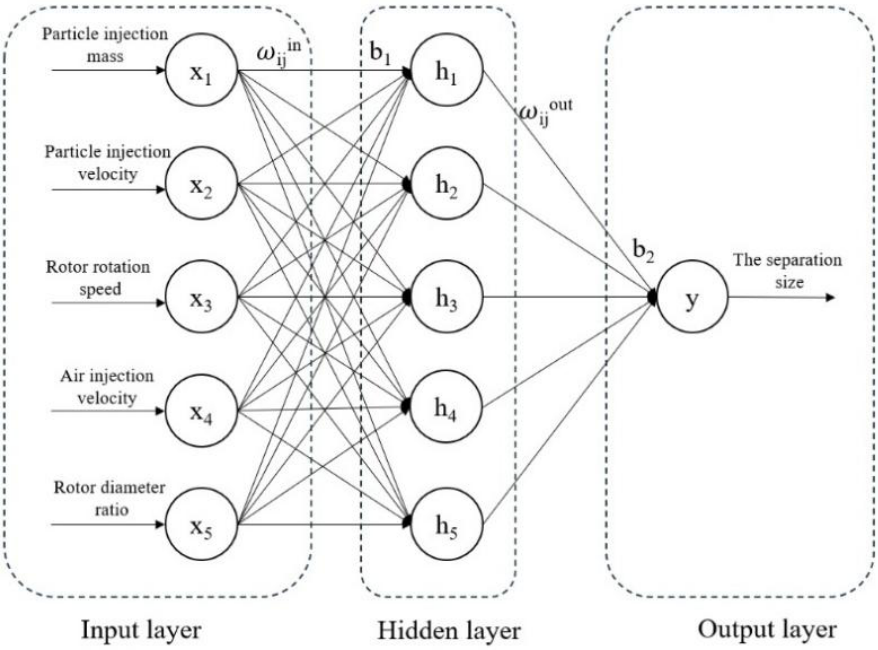

Fig. 4. Diagram of the structure of a BP neural network

As illustrated in Fig. 5, the developed BP neural network model with a 5-5-1 architecture demonstrates strong capabilities for nonlinear fitting. The regression analysis revealed that the correlation coefficient of this BP neural network model exceeds 98% across the training set, validation set, test set, and the entire dataset. The results indicate a strong correlation between the predictions generated by the BP neural network model and the values obtained from simulation. Evaluation of the performance on validation and test sets demonstrates the generalization capability and stability of BP neural network prediction models.

3.4.2. Response surface methodology (RSM) fitting

Based on 60 sets of simulation data, the system was modeled and optimized utilizing the Response Surface Methodology (RSM). The factors considered in this analysis are core simulation parameters. The separation size (d_c) served as the response variable in this study. The relationship between the factors and responses was elucidated through the application of polynomial analysis. During the analysis, coded data were employed to mitigate the impact of varying scales and units of measurement on the data analysis process. The analysis of variance (ANOVA) was employed to evaluate the model's error and uncertainty. The findings from the data analysis are presented in Table 3. The model under the Quadratic condition demonstrates the highest adjusted R^2 value of 0.9559, with a sequential p-value of less than 0.0001. This indicates a greater overall statistical significance for the model. In contrast, both the linear and two-factor interaction (2FI) models exhibit some explanatory power; however, their predictive capabilities are considerably weaker than those of the quadratic model. The cubic and quartic models demonstrate an overall lack of statistical significance.

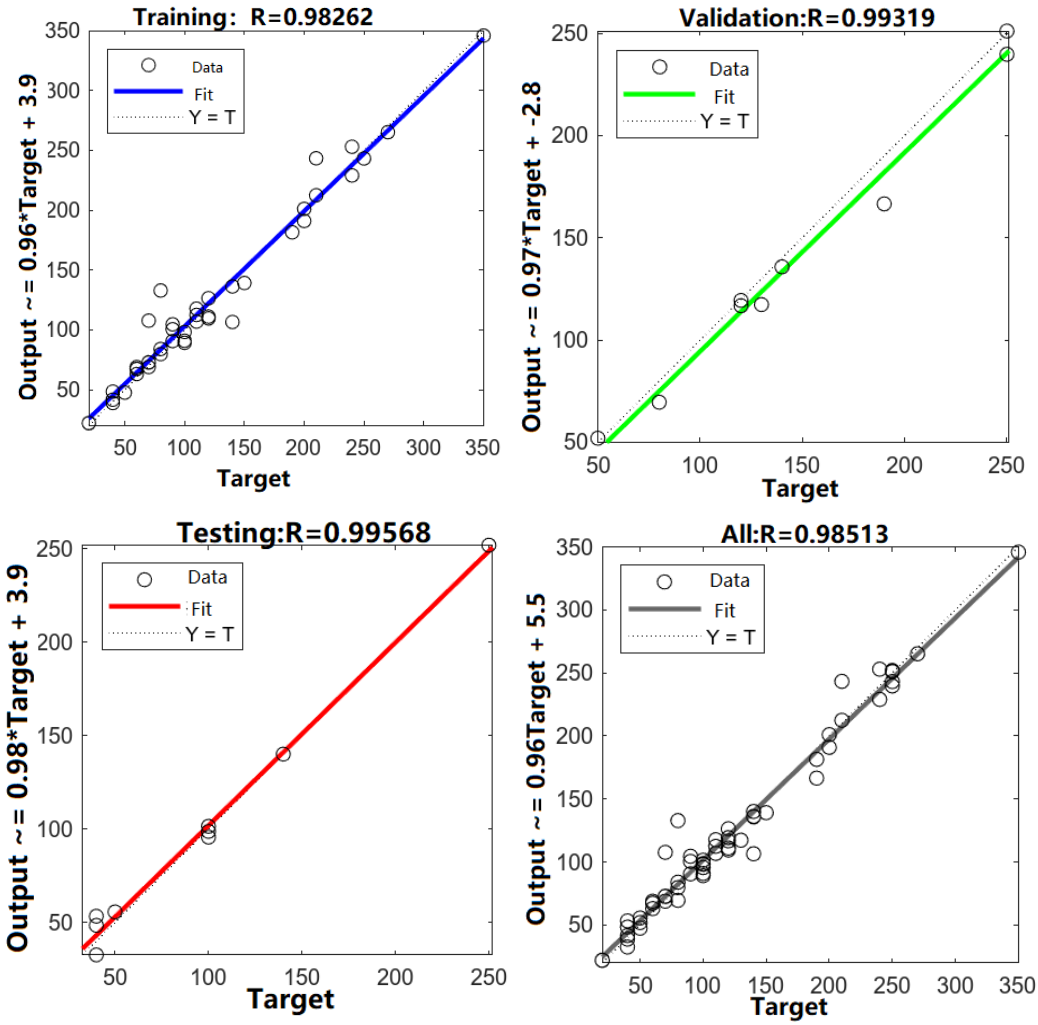

Fig. 5. Results of regression analysis for the BP neural network model based on 60 sets of simulation data

Table 3. Comparative analysis of response surface models based on 60 sets of simulation results

Source	Sequential p-value	Adjusted R^2	Predicted R^2
Linear	< 0.0001	0.7738	0.7359
2FI	0.0005	0.8560	0.7663
Quadratic	< 0.0001	0.9559	0.9241
Cubic	0.8947	0.9176	
Quartic		1.0000	

4. Comparison of joint modeling programs and effects

4.1. Joint modeling program

To emphasize the advantages of BP neural network, which can adaptively capture arbitrary continuous nonlinear relationships between input variables through the activation functions of nodes in the implicit layer (Mehrkash and Santini-Bell, 2025), as well as the benefits of response surface that provides explicit mathematical expressions and visual representations for intuitive analysis of parameter interactions (Liu et al., 2025). A data processing program for joint BP-RSM modeling has been developed, as illustrated in Fig. 6.

Firstly, a total of 60 sets of simulation data were used, covering the core simulation parameters and the separation size (d_c). These data were input into a BP neural network model, which was subsequently trained to construct a prediction model with the separation size (d_c) as the output. Subsequently, a total of 12,150 parameter space nodes were generated through uniform interpolation within the model

prediction domain. These nodes were then input into the trained BP neural network model to yield 12,150 sets of virtual experimental data based on predictions. Following this, the virtual experimental data were incorporated into the response surface model. Finally, the response surface plots derived from 12,150 sets of virtual experiments were generated through polynomial fitting, as illustrated in Fig. 7(a). By analyzing the results of the Response Surface Methodology (RSM), one can elucidate the relationship between various factors, thereby enhancing the understanding of underlying objective principles (Song et al., 2024).

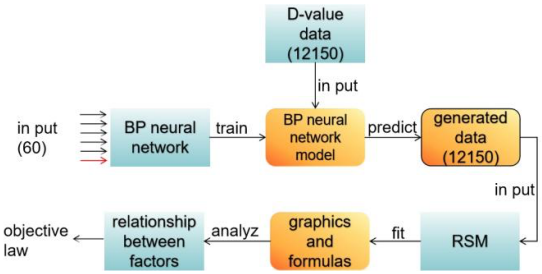

Fig. 6. Data processing framework for joint BP-RSM modeling

To compare the differences between the BP-RSM method and traditional Response Surface Methodology (RSM), we directly employed the Response Surface Methodology (RSM) to fit polynomials to the original 60 sets of simulation data. The resulting response surfaces are presented in Fig. 7(b).

To assess the robustness of the method, the original dataset was further reduced by 50%, retaining 30 sets. Subsequently, both the BP-RSM method and traditional RSM were employed to construct comparative models, resulting in two sets of response surface distributions, as illustrated in Fig. 7(c) and Fig. 7(d).

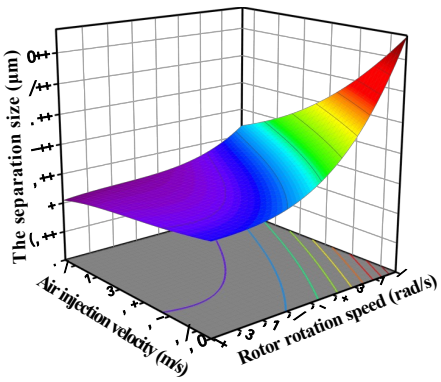

(a) The BP-RSM method with 60 data sets

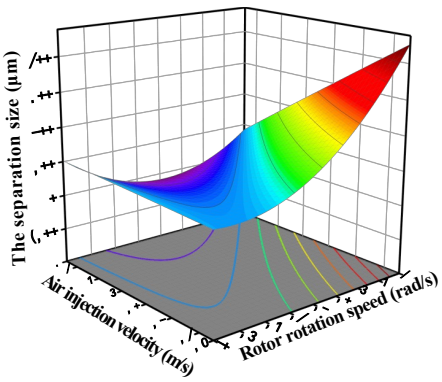

(b) Traditional RSM with 60 data sets

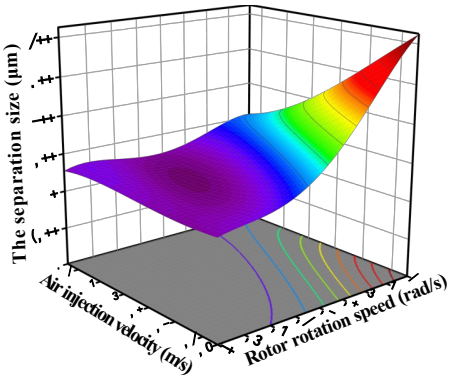

(c) The BP-RSM method with 30 data sets

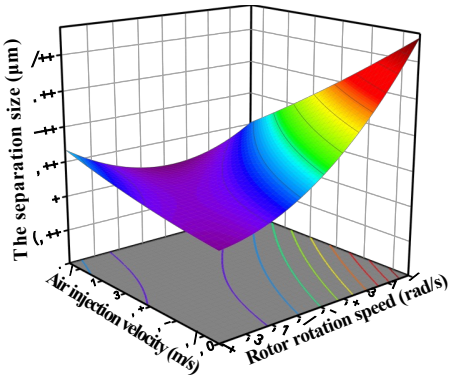

(d) Traditional RSM with 30 data sets

Fig. 7. Comparison of the BP-RSM method with traditional RSM for analyzing response surface modeling of v_g-ω interactions

To quantitatively assess the fitting accuracy of four methods—namely, the BP-RSM method with 60 data sets, the BP-RSM method with 30 data sets, traditional RSM with 60 data sets, and traditional RSM with 30 data sets—the integrated R^2 and predicted R^2 values from direct fitting for each of these programs were evaluated. And the fitting accuracy of the BP neural network model in predicting virtual experimental data was compared under two conditions: 30 sets of data and 60 sets of data. To evaluate the fitting accuracy of four methods relative to the original dataset consisting of 60 sets, Eq. 8 (He et al., 2025) was employed for comparison. The results of this comparison are presented in Table 4.

$$R^2 = 1 - \frac{\sum_{i=1}^{n}(y_i - \hat{y}_i)^2}{\sum_{i=1}^{n}(y_i - \bar{y}_i)^2} \tag{8}$$

Table 4. Comparison of goodness-of-fit between the BP-RSM method and traditional RSM

group	Integrated R^2 of direct fitting	Predicted R^2 of direct fitting	Integrated R^2 of (RSM/BP) fitting	Predicted R^2 of (RSM/BP) fitting	Validated R^2 of joint fitting
The BP-RSM method (60 data sets)	97.05%	99.14%	99.76%	99.75%	96.82%
Traditional RSM (60 data sets)	97.08%	92.41%	/	/	97.08%
The BP-RSM method (30 data sets)	98.98%	98.18%	97.01%	96.93%	93.08%
Traditional RSM (30 data sets)	98.81%	66.71%	/	/	93.52%

4.2. Comparison of the BP-RSM method with Traditional RSM

4.2.1. Integrated R^2 analysis of direct fit

As illustrated in the first and second columns of Table 4, the integrated R^2 values for direct fit using the BP neural network method and traditional RSM are 97.05% and 97.08%, respectively, under conditions involving a large sample size of 60 sets of data. The empirical fitting abilities of both models are demonstrated to be comparable, achieving values of 98.98% and 98.81%, respectively, under the condition of a small sample size (30 sets) of data.

However, the predictive performances exhibit significant variations: in the full data prediction involving 60 sets, the BP neural network method achieves a direct fit prediction R^2 of 99.14%, representing an improvement of 6.73% over traditional RSM, which stands at 92.41%. In the context of small-sample prediction involving 30 sets, the BP neural network method demonstrates a remarkable retention of 98.18% in direct-fit prediction R^2. In contrast, traditional RSM experiences a significant decline to 66.71%, reflecting a decrease of 31.47%. The results presented above indicate that the BP neural network method effectively mitigates the issue of overfitting through its nonlinear generalization mechanism. Furthermore, it demonstrates enhanced engineering applicability in complex working conditions characterized by small sample sizes.

4.2.2. An analysis of the validity in joint modeling

As illustrated in columns 3 and 4 of Table 4, based on the 12,150 sets of virtual data generated by the BP neural network method, the Response Surface Methodology (RSM) demonstrates a very high fitting ability under the large sample (60 sets-12,150 sets) condition, and the integrated R^2 (RSM/BP) and

predicted R^2 (RSM/BP) of the RSM for the virtual experimental data generated by the BP method are respectively 99.76% and 99.75%, indicating that the response surface model can accurately resolve the prediction law of the BP neural network model. However, under the small sample (30 sets-12,150 sets) condition, the fitting of the response surface, although showing clear validity, showed a significant performance degradation, with its integrated R^2 (RSM/BP) and predicted R^2 (RSM/BP) dropping to 97.01% and 96.93%, respectively, indicating that the RSM is not sufficiently adaptive to the larger nonlinear fluctuations of the BP neural network.

The fifth column of Table 4 provides a comparative analysis of the effectiveness of various models in validating the original experimental data. For the large sample condition involving 60 sets, both traditional RSM and the BP-RSM method demonstrated comparable results in terms of goodness-of-fit. The joint fit validation R^2 values were recorded at 97.08% for traditional RSM and 96.82% for the BP-RSM method, respectively. In the small sample condition (30 sets), both traditional RSM and the BP-RSM method exhibited a decrease in goodness of fit. The joint fit validation R^2 values were recorded at 93.52% for traditional RSM and 93.08% for the BP-RSM method, respectively. This suggests that, although there is a slight loss in accuracy due to the incorporation of the response surface model, the BP-RSM method serves as a crucial analytical tool for optimizing process parameters. This is achieved through the enhancement of virtual data with explicit mathematical representation, particularly improving prediction accuracy under neural network constraints. Such capabilities underscore its significant utility in engineering applications.

4.2.3. Comparative analysis of response surface plots

As illustrated in Fig. 7, the BP neural network model demonstrates graphical explicit results through the integration of BP neural network and response surface joint modeling, as depicted in Fig. 7(a) and Fig. 7(c). We also observe that the response surface results obtained from traditional RSM and the BP-RSM method exhibit significant differences in the region characterized by air injection velocity (v_g) and high rotor rotation speed (ω). When the air injection velocity (v_g) is less than 6 m/s, the separation size (d_c) predicted by traditional RSM, as illustrated in Fig. 7(b) and Fig. 7(d), appears to exhibit a non-physical curved surface depression that decreases with rotor rotation speed (ω). At v_g of 3 m/s, the separation size (d_c) reaches a maximum of 100 μm at the highest rotor rotation speed (ω), subsequently increasing with air injection velocity (v_g). Notably, a minimum value of -10 μm is observed, as shown in Fig. 7(b).

For the model comprising 30 sets, the separation size (d_c) attains a maximum of 110 μm at the highest rotor rotation speed (ω). Additionally, there exists a minimum value approaching 0 as the air injection velocity (v_g) increases, as illustrated in Fig. 7(d), which contradicts the established physical principles governing particle separation mechanisms (Shang et al., 2024). In contrast, the BP-RSM method utilizing 30 sets of experimental data effectively mitigates the reduction in the separation size (d_c), as illustrated in Fig. 7(c). This is achieved through the nonlinear compensation provided by the BP neural network, which incorporates an extension of virtual data and adheres strictly to the physical constraint (d_c>0). Under the condition of 60 sets of experimental data as illustrated in Fig. 7(a), the previously observed depressed region was completely eliminated, resulting in a higher degree of concordance with industrial observations (Pareek and Sankhla, 2021). The comparison of the fitting results confirms the physical validity and predictive stability of the BP-RSM method under complex operating conditions.

The BP-RSM method effectively generates virtual data to construct the response surface model using a BP neural network. This approach addresses the issues of negative value paradoxes and surface distortions that arise from traditional methods when working with limited sample sizes. Furthermore, it demonstrates enhanced stability in scenarios where experimental data is scarce. Meanwhile, the explicit formulation of the response surface output, along with its corresponding graphical representation, offers intuitive analytical tools and theoretical support for optimizing the operational parameters of separators.

5. Industrial experimental verification

5.1. Experimental equipment and raw materials

A self-made experimental mill (with a rotor diameter of 0.6 m and a height of 0.3 m) was used for air

separation, and iron ore powder (with a density of 5000 kg/m³) was used as the raw material.

5.2. Experimental procedure

5.2.1. Industrial experiment

The iron ore powder was classified through 1.3 mm, 0.7 mm, 0.3 mm, 0.15 mm and 0.075 mm vibrating screens, and then mixed with 40 kg of samples in the proportion shown in Table 5. Then, the sorting is carried out under the air selection parameters in Table 6. After the fine powder in the mill was completely sorted, the machine was shut down. About 5 kg of the material was collected at the sampling port of the cyclone cylinder. 2.5 kg of the sample was sieved and weighed at 0.075 mm. The results are shown in Table 8.

Table 5. Particle size distribution of iron ore powder

Particle size range (mm)	>1.2	>0.6	>0.3	>0.15	>0.075	<0.075
Mass fraction (%)	30.3	20.7	16.6	11.6	8.3	12.5

Table 6. Air selection operation parameters

Parameter	Set value
v_g (m/s)	1.08
ω (rad/s)	7.85

5.2.2. Simulation experiment

Based on the industrial particle size distribution (Table 5), 12 groups of particle size intervals (d_p) (Table 7) were set, and the total particle injection mass (m_p) was 20 kg/s to conduct the transient simulation of air-solid two-phase flow.

Table 7. Particle injection parameters

d_p(mm)	0.04	0.07	0.08	0.11	0.2	0.25	0.4	0.5	0.8	1	1.4	1.6
m_p (kg/s)	1.25	1.25	0.83	0.83	1.16	1.16	1.66	1.66	2.07	2.07	3.13	3.13
Mass fraction (%)	6.25	6.25	4.15	4.15	5.80	5.80	8.30	8.30	10.35	10.35	15.65	15.65

5.3. Experimental results

5.3.1. Industrial experiment results

The particle size distribution of the finished cyclone cylinder is shown in Table 8.

Table 8. The particle size distribution of the finished cyclone cylinder

Particle size range (mm)	>0.6	>0.3	>0.15	>0.075	<0.075
Mass fraction (%)	0	0	0	20	80

5.3.2. Simulation experiment result

The particle escape rate (α) is shown in Table 9.

Table 9. Particle escape rate (α). (v_g=1.08 m/s, ω=7.85 rad/s)

d_p (mm)	0.04	0.07	0.08	0.11	0.2	0.25	0.40	0.50	0.80	1	1.4	1.6
α	1.0	1.0	0.5	0	0	0	0	0	0	0	0	0

5.4. Model verification

5.4.1. Verification method

The accuracy of the model was verified based on the proportion of particles with a particle size of less than 0.075 mm in the industrial experiment.

$$T = \frac{\sum(m_p \times \alpha \times t)_{d_p<0.075mm}}{U} \times 100\% \tag{9}$$

where: U represents the total escape mass and T represents the proportion of simulation products.

5.4.2. Verification result

As shown in Table 10, the absolute deviation between the simulation results and the industrial data results is less than 6%, and the relative deviation is +7.1%, which is within the allowable error range of the project. The reliability of the model has been verified, proving that the model has an excellent predictive ability for the powder selection process.

Table 10. Verification result

Parameter	Industrial experiment	Simulation experiment results	Absolute deviation	Relative deviation
Proportion of particles < 0.075 mm (%)	80	85.7	+5.7%	+7.1%

6. Analysis and discussion of results

6.1. Relevance analysis

To attain more efficient and targeted data analysis, as well as to uncover the correlations among the data, it is essential to analyze the relationships between the responses of various factors. As indicated by the analysis of variance (ANOVA) results presented in Table 11, rotor rotation speed (ω) at C-C, air injection velocity (v_g) at D-D, and rotor diameter ratio (d/d_0) at E-E demonstrated highly significant main effects on the response variable—the separation size (d_c). The corresponding F-values were 64,328.02, 34,548.89, and 14,868.99 respectively (with mean squares of 2.363E +06, 1.269E +06, and 5.461E +05), which are one to three orders of magnitude greater than those for particle injection mass (m_p) at A-A (F=76.28) and particle injection velocity (v_p) at B-B (F=554.16). This suggests that parameters C-C, D-D, and E-E are critical regulatory factors influencing the outcomes observed in this study.

The analysis of interaction effects further indicated that the coupling between rotor rotation speed (ω) and air injection velocity (v_g) (CD, F=23,469.34), the relationship between air injection velocity (v_g) and rotor diameter ratio (d/d_0) (DE, F=9,013.56), as well as the interaction between rotor rotation speed (ω) and rotor diameter ratio (d/d_0) (CE, F=2,773.91), all reached a highly significant level ($p<0.0001$). The mean squares for these interaction terms were 8.620E+05, 3.311E+05, and 1.019E+05, respectively.

Table 11. Analysis of correlation among factors

Source	Mean Square	F-value	Source	Mean Square	F-value	Source	Mean Square	F-value
A-A	2801.65	76.28	AB	195.63	5.33	BD	19280.04	524.93
B-B	20353.53	554.16	AC	18664.39	508.17	BE	21.42	0.5831
C-C	2.363E+06	64328.02	AD	16275.42	443.12	CD	8.620E+05	23469.34
D-D	1.269E+06	34548.89	AE	449.93	12.25	CE	1.019E+05	2773.91
E-E	5.461E+05	14868.99	BC	12934.14	352.15	DE	3.311E+05	9013.56

6.2. Key factors extraction

The rotor rotation speed (ω) and rotor diameter ratio (d/d_0) exhibit relative stability for each individual device. However, the distribution characteristics of air injection velocity (v_g) demonstrate significant

nonuniformity, which can be attributed to the perturbation effects present in the flow field within the vertical roller mill region, as illustrated in Fig. 8. The high-velocity airflow in the nozzle ring region is divided into multiple zones of varying velocities as it circulates around the vertical roller mill rollers. This airflow maintains a distinct difference between the high and low velocity zones while spiraling upward, as illustrated in Fig. 8(a). Next, after passing through the throat opening region, the airflow is influenced by the negative pressure at this location. This interaction generates a low-velocity zone at the bottom of the rotor area, which is further guided by both the resistance of the flow field and the wall. Consequently, a low-velocity zone also forms at the top of the rotor area, as illustrated in Fig. 8(b). It ultimately generates characteristics of circumferential and axial velocity inhomogeneity at the interface between the outlet of the vertical roller mill and the inlet of the separator, as illustrated in Fig. 8(c). This non-uniformity in the flow field directly induces fluctuations in particle trailing, which serves as a critical factor contributing to the instability of the separation size (d_c).

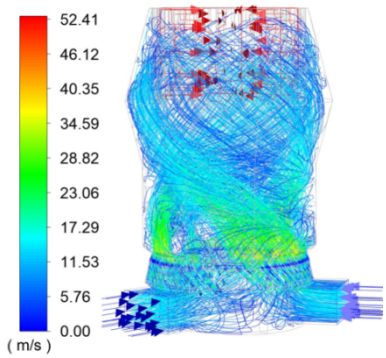

(a) Vertical roller mill body air trajectory line

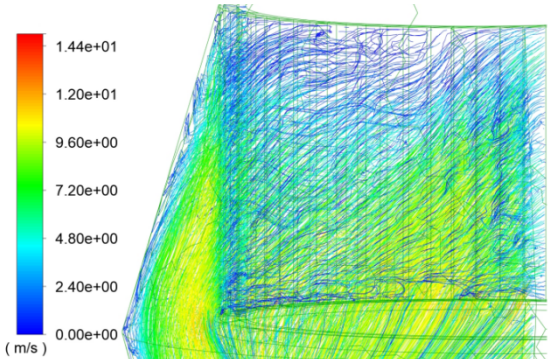

(b) Inlet air trajectory line of separator

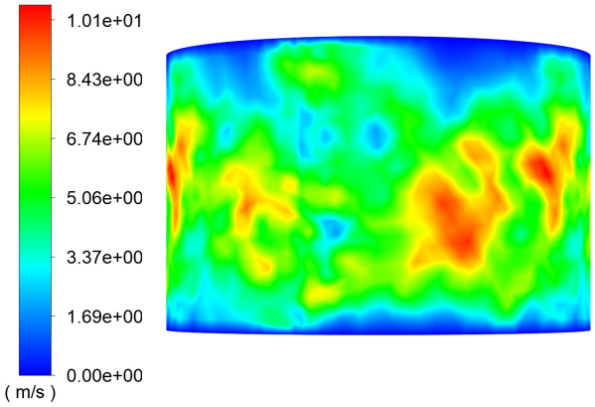

(c) Inlet air velocity cloud of separator

Fig. 8. Perturbation effect of the flow field in the roller region of a vertical roller mill

For this reason, to achieve a stable and accurate evaluation of the separation size (d_c), an analytical framework was established with the air injection velocity (v_g) as the key variable and the separation size (d_c) as the target response. In the context of clear air injection velocity (v_g) and the separation size (d_c), a more distinct relationship can be observed between rotor rotation speed (ω) and the rotor diameter ratio (d/d_0). Consequently, the design of rotor rotation speed (ω) is fundamentally based on the rotor diameter ratio (d/d_0). To achieve more intuitive conditions for mechanistic analysis, the rotor diameter ratio (d/d_0), which is associated with the equipment structure, was selected for optimization. The rotor rotation speed (ω) served as the adjustment variable, while the particle injection velocity (v_p) and particle injection mass (m_p) were utilized as auxiliary reference variables.

There are variations in the width of the contours representing air injection velocity (v_g) under different conditions. The broader region of contours indicates a relatively weak response in the separation size (d_c) when subjected to significant variations in air injection velocity (v_g). The area characterized by elevated contour gradients, conversely, suggests that the condition exhibits a more pronounced response to variations in air injection velocity (v_g). Therefore, the contour width of the

separation size was utilized as the primary evaluation criterion.

In summary of the aforementioned characteristics, a three-dimensional response surface analysis framework has been developed, incorporating three factors and multiple reference variables, as illustrated in Table 12.

Table 12. 3D response surface analysis program

Factors	Impact
Air injection velocity (v_g)	Essential Variables
The separation size (d_c)	Response Target
Rotor diameter ratio (d/d_0)	Optimization Objectives
Rotor rotation speed (ω)	The following variable
Particle injection velocity (v_p)	Auxiliary reference variable
Particle injection mass (m_p)	Auxiliary reference variable
Contour width of the separation size (d_c)	Fundamental Evaluation Criteria

6.3. Analysis of joint modeling results

The target separation size (d_c) of 40-60 μm was initially established. Under this condition, the objective was to obtain results characterized by broader contours within the range of 40-60 μm. Afterward, the focus of the analysis is clarified. The air injection velocity (v_g) serves as the invariant coordinate, while the rotor rotation speed (ω) and rotor diameter ratio (d/d_0) are paired coordinates. Additionally, the particle injection mass (m_p) and particle injection velocity (v_p) are adjusted coordinates utilized for conducting response surface analysis. Consequently, a response surface contour plot is generated, as illustrated in Fig. 9. Under the conditions of particle injection mass (m_p) at 27.5 kg/s, particle injection velocity (v_p) at 14 m/s, and rotor rotation speed (ω) at 12.8 rad/s, it is observed that the region of air injection velocity (v_g) corresponding to the separation sizes (d_c) ranging from 40 to 60 μm exhibits a tendency to initially increase and subsequently decrease as the rotor diameter ratio (d/d_0) increases.

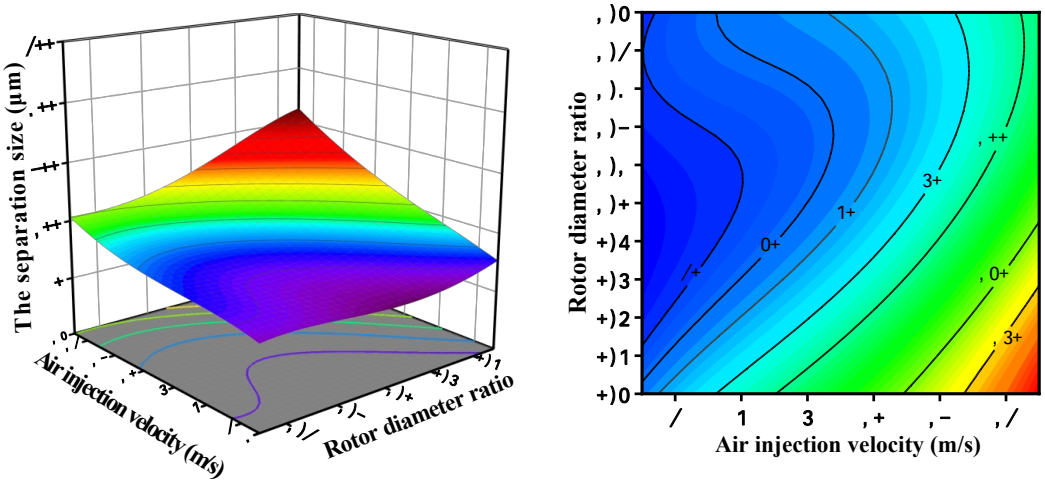

(a) 3D response surface plot (b) Response surface contour plot

Fig. 9. Analyzing response surface modeling of v_g-(d/d_0) interactions

As illustrated in Fig. 10(a), the maximum air injection velocity (max v_g) and the minimum air injection velocity (min v_g) corresponding to the separation size (d_c) of 40-60 μm exhibit variation with respect to the rotor diameter ratio (d/d_0). The distance between these two curves reaches its maximum when the rotor diameter ratio (d/d_0) is within the range of 1.2-1.4. Further, Fig. 10(b) illustrates the difference in maximum and minimum air injection velocities, as well as the ratio of maximum to minimum air injection velocities, corresponding to the separation size (d_c) range of 40-60 μm. This variation is analyzed in relation to the rotor diameter ratio (d/d_0). Notably, there exists an optimal value that corresponds to a peak velocity within the specified interval for the separation sizes (d_c). In terms of

both the difference in air injection velocity and the ratio of air injection velocities, the maximum values are observed under conditions where the rotor diameter ratio (d/d_0) ranges from 1.2 to 1.4. That is, under the condition that the rotor diameter ratio (d/d_0) ranges from 1.2 to 1.4, a more precise separation size (d_c) can be achieved. At this point, the diameter of the separator should be between 6038 mm and 7045 mm.

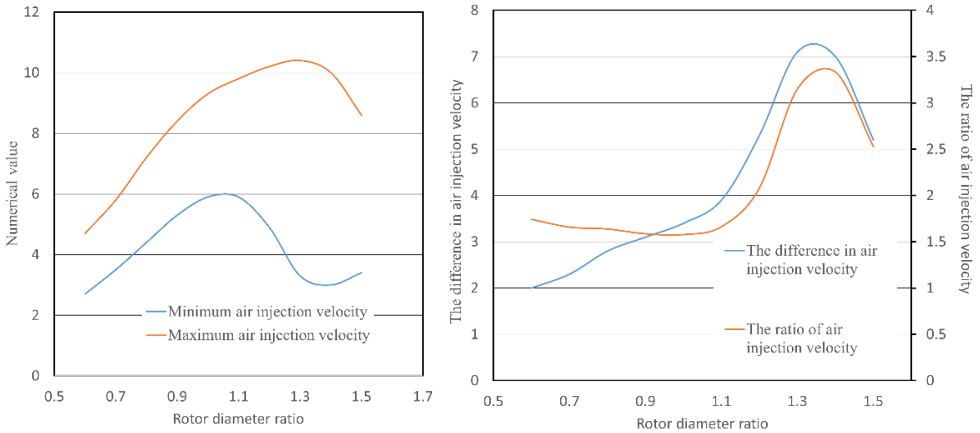

(a) Curve of velocity differences (b) Curve of the velocity difference/ratio

Fig. 10. The relationship between air injection velocity (v_g) and rotor diameter ratio(d/d_0) for the separation size(d_c) of 40-60 μm

6.4. Mechanism of the nonlinear effect of inter-blade flow field on the separation size

Since the rotor is designed as a geometrically scaled model, under ideal conditions—where the particle injection mass (m_p), particle injection velocity (v_p), and air injection velocity (v_g) remain constant—it can be inferred from Eq. 4 that the separation size (d_c) in both the direction of rotor rotation speed (ω) and along the diameter should exhibit a consistent scaling relationship. However, the data analysis results consistently indicated a significant nonlinear shift in the separation size (d_c). This phenomenon suggests that the vortex behavior generated by the moving blades substantially interferes with the particle separation process. As illustrated in Fig. 11, the strength of the vortex formed between the moving blades exhibits a gradual enhancement with an increase in the rotor diameter ratio (d/d_0) and a decrease in air injection velocity (v_g).

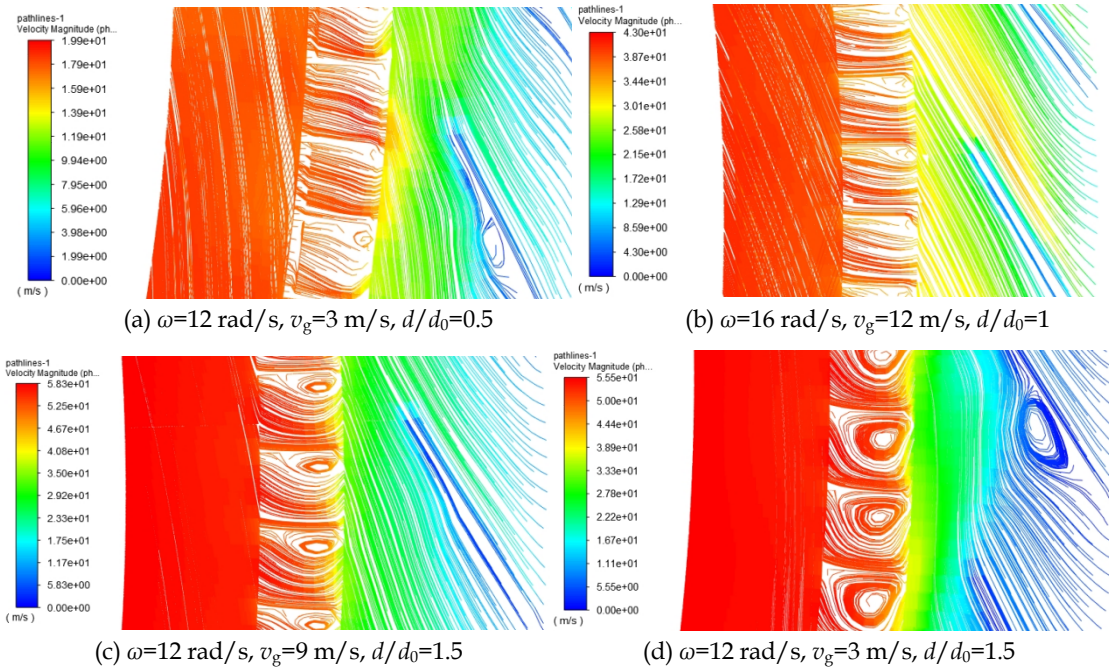

(a) ω=12 rad/s, v_g=3 m/s, d/d_0=0.5 (b) ω=16 rad/s, v_g=12 m/s, d/d_0=1

(c) ω=12 rad/s, v_g=9 m/s, d/d_0=1.5 (d) ω=12 rad/s, v_g=3 m/s, d/d_0=1.5

Fig. 11. Intensity of the vortex between moving blades under varying conditions of ω, v_g, d/d_0

Under the condition of a specific separation size (d_c), it is essential to maintain the balance of centrifugal force. According to Eq. 1, as the rotor diameter ratio (d/d_0) increases, although the angular velocity decreases, the linear velocity simultaneously increases. This leads to an increased velocity gradient between the moving and static blades, resulting in enhanced vortex strength between them. The vortex generated between the blades establishes a low-pressure zone that facilitates the intake of particle-laden air into the space between the rotor blades. This phenomenon results in an increased velocity of particles as they traverse through the moving blades, ultimately leading to their expulsion at the outlet due to the accelerating effect of the vortex. Due to the varying responses of different particle sizes to vortex traction, as described by Eq. 2 and Eq. 5, the acceleration and displacement of smaller particles are greater than those of larger particles. This differential behavior is advantageous for the separation of particles based on size. At this stage, under conditions of equilibrium for equal centrifugal force separation, the air injection velocity (v_g) is decreased. As a result, the equi-separated particles demonstrate a slight deviation towards the lower-velocity region; however, the range of equal separation sizes becomes broader. As illustrated in Fig. 12, particles with sizes ranging from 10-50 μm exhibit a distinct positional variation after traversing the vortex generated by the moving blades. Smaller particles are more likely to exit the vortex region along with the airflow movement, whereas larger particles tend to be re-captured by the vortex due to the influence of centrifugal force.

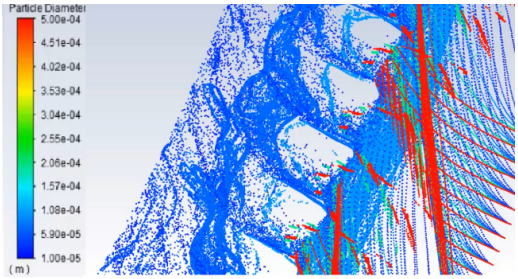

Fig. 12. Dynamics of 10-50 μm particles under vortex action

When the rotor diameter ratio (d/d_0) exceeds 1.2, the vortex intensity between the moving blades continues to enhance. Consequently, the separation capability of the rotor itself is progressively diminished, leading to a shift in the separation point curve towards the low-speed zone. Additionally, the band of equal separation sizes becomes narrower. The observed decline in separation capability can be attributed to the imbalance phenomenon in the contributions of vortex and rotor separation, which arises from the enhancement of vortex separation capabilities. On one hand, the unstable and non-uniform characteristics of the vortex between the blades facilitate the breakthrough of larger particles (d_p>60 μm) against the centrifugal force-dominated high-velocity laminar flow separation zone. This occurs under conditions of stronger vortex acceleration, allowing these particles to enter the exit channel where air injection velocity (v_g) is relatively low. Consequently, this phenomenon results in a higher proportion of large particles escaping. On the other hand, the low-pressure zone created by the vortex at the rear of the blades exerts a negative pressure adsorption effect on large particles that accumulate in the region between the moving and static blades, such as those illustrated in Fig. 13. This phenomenon leads to an elevation of the base of potentially escaping large particles. At the same time, the proportion of large particles within the vortex region increases, leading to a localized enrichment. This phenomenon results in an elevated trailing force acting on the large particle population and consequently a higher proportion of escaping particles. The superposition of the two aspects results in an increased proportion of larger particles escaping under identical centrifugal force equilibrium conditions. This phenomenon leads to a deterioration in escape stability and causes a shift of equi-separated particles towards the low-velocity zone, while simultaneously narrowing the band of equal separation sizes.

It is evident that the vortex behavior occurring between the moving blades significantly influences the separation size (d_c). Effectively harnessing this property can facilitate achieving a higher adaptability of air injection velocity (v_g). Under the current conditions regarding rotor diameter, the optimal width of the band corresponding to equal separation sizes—indicative of superior air speed adaptability—is achieved by expanding the rotor diameter to between 1.2 and 1.4 times its original size.

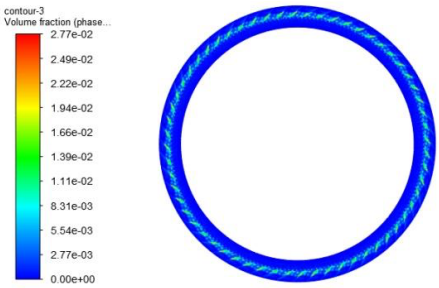

Fig. 13. Large particle collection area between the moving and static blades

6. Conclusions

The study was based on CFD-DDPM to obtain 60 sets of flow field data and establish a joint BP-RSM modeling model. The experiments demonstrate that the BP-RSM method and traditional RSM exhibit similar validation R^2 values of 96.82% and 97.08%, respectively, under the condition of utilizing 60 data sets. However, the BP neural network method has a higher prediction R^2 (99.14%). This advancement effectively addresses the shortcomings of conventional methods regarding the distortion of separation features in low-speed zones. The model offers both high accuracy and a clear expression program for the flow field analysis of separators, thereby broadening the application of numerical simulation and data analysis in the optimization of industrial equipment.

By analyzing the key factors within the model of rotor diameter ratio (d/d_0), air injection velocity (v_g), and the separation size (d_c), it can be found that the gradient of the separation size (d_c) in the direction of air injection velocity (v_g) is significantly different with the rotor diameter ratio (d/d_0). At the target separation size of ±10 μm, the gradient of separation size (d_c) exhibited an initial increase followed by a subsequent decrease as the rotor diameter ratio (d/d_0) increased. The inflection point is located in the interval 1.2-1.4 times (6038mm-7044mm) when d_0 is 5023mm.This observation suggests that the separation accuracy at this scale is enhanced under conditions characterized by multifactorial coupling. A novel analytical approach for optimizing the diameter parameters of separators is presented, drawing on insights gained from linear scale scaling in traditional design practices.

The study further elucidates the limitations of the conventional centrifugal-tracer binary model by incorporating the influence of vortices generated between the moving blades, which arise from the velocity gradient between the moving and static blades. This factor significantly impacts the sorting efficiency of particles. The secondary vortex field induced by the velocity gradient of both the moving and static blades enhances the inertial separation efficiency of particles. However, it also leads to fluctuations in the separation size (d_c). The mechanistic model effectively elucidates the anomalous inflection point phenomenon observed in the curves of rotor diameter ratio (d/d_0) and the separation size (d_c) during data analysis. Furthermore, it offers a novel regulatory perspective for the design of high-precision separation equipment.

Acknowledgments

National Natural Science Foundation of China (No.52475354); Collaborative Education Project of the Ministry of Education (No.221001414112514).

Reference

ADNAN, M., SUN J, AHMAD, N., et al., 2021. *Comparative CFD modeling of a bubbling bed using a Eulerian–Eulerian two-fluid model (TFM) and a Eulerian-Lagrangian dense discrete phase model (DDPM)*, Powder Technology, 383, 418-432.

ALTUN, D., BENZER, H., AYDOGAN, N., et al., 2017. *Operational parameters affecting the vertical roller mill performance*, Minerals Engineering, 103-104, 67-71.

BAGHERZADEH, A., DARBANDI, M., BAREZBAN M.B., 2024. *Numerical simulation of particle separation in a two-phase flow passing through a vortex-based air classifier using Eulerian–Lagrangian DDPM approach*, Powder Technology, 445, 120036.

DOBSON, J.E., 2023. *On reading and interpreting black box deep neural networks*, International Journal of Digital Humanities, 5(2-3), 431-449.

ESMAEILPOUR, M., MOHEBBI, A., GHALANDARI, V., 2024. *CFD simulation and optimization of an industrial cement gas–solid air classifier*, Particuology, 89, 172-184.

FATAHI, R., ABDOLLAHI, H., NOAPARAST, M., et al., 2025. *Modeling the working pressure of a cement vertical roller mill using SHAP-XGBoost: A "conscious lab of grinding principle" approach*, Powder Technology, 457, 120923.

FATAHI, R., POURNAZARI, A., SHAH, M.P., 2022. *A cement Vertical Roller Mill modeling based on the number of breakages*, Advanced Powder Technology, 33(10).

GENG P H, CHEN Y X, YAO Y F, et al., 2021. *Mathematical modeling study based on the particle classification process of the vertical mill classifier*, Chinese Journal of Process Engineering, 21(06), 680-686.

GIDASPOW, D., BEZBURUAH, R., DING J., 1992. *Fluidization VII, Proceedings of the 7th Engineering Foundation Conference on Fluidization, Hydrodynamics of circulating fluidized beds, kinetic theory approach*, 75-82.

HE W, TANG H, LI J, et al., 2025. *Using the coefficient of determination to identify injury regions after stroke in pre-clinical FDG-PET images,* Computers in Biology and Medicine, 184, 109401.

HU H, LI Y, JIN H, et al., 2025. *Analysis of the gas-solid two-phase flow characteristics and the impact of key structural parameters on the separation performance of medium-speed coal mills*, Advances in Engineering Software, 204, 103896.

HU H, LI Y, LU Y, et al., 2025. *Study of influencing factors of performance in novel vertical roller mills*, Advances in Engineering Software, 202.

HUANG H, LI Y, LU Y, et al., 2024. *Numerical Study of Flow Field and Particle Motion Characteristics on Raw Coal Vertical Roller Mill Circuits*, Minerals Engineering, 218, 108997.

HUANG R, MA Y, LI H, et al., 2023. *Operation parameters multi-objective optimization method of large vertical mill based on CFD-DPM,* Advanced Powder Technology, 34(6), 104014.

ISMAIL, F.B, AL-MUHSEN, N.F.O., HASINI, H., et al., 2022, *Computational Fluid Dynamics (CFD) investigation on associated effect of classifier blades lengths and opening angles on coal classification efficiency in coal pulverizer*, Case Studies in Chemical and Environmental Engineering, 6, 100266.

LI H, He Y, SHI F, et al., 2016. *Performance of the static air classifier in a Vertical Spindle Mill*, Fuel, 177, 8-14.

LI H, SONG Z, WANG R, et al., 2024. *Study on the influence of baffle height and angle on the performance of coarse powder separator in power plant based on CFD-DPM method*, International Journal of Heat and Fluid Flow, 109, 109523.

LIU J, YANG D, MA W, et al., 2025. *Optimization of biomimetic weave parameters using response surface methodology to improve tribological performance of HSLT-Q235*, Applied Surface Science, 696, 162894.

MEHRKASH, M., SANTINI-BELL, E., 2025. *Robustness analysis of multi-layer feedforward artificial neural networks for finite element model updating,* Applied Soft Computing, 171, 112799.

PAREEK, P., SANKHLA, V.S., 2021. *Review on vertical roller mill in cement industry & its performance parameters*, Materials Today: Proceedings, 44, 4621-4627.

SONG L, XIE J, JIANG Q, et al., 2024. *A back-propagation neural network optimized by genetic algorithm for rock joint roughness evaluation*, Journal of Rock Mechanics and Geotechnical Engineering.

SHANG M, KE X, XIAO H, et al., 2024. *Experimental investigation on the preparation of macroscopic 0–1 mm powdered coal by a vertical spindle mill*, Chemical Engineering Research and Design, 208, 74-80.

SUN S F, WANG W B, LÜ Y, 2012. *Study on the speed characteristics of a vortex air classifier*, China Non-metallic Mineral Industry Herald, (4), 36-38 + 47.

TAGHINEZHAD, J., ABDOLI, S., SILVA V., et al., 2023. *Computational fluid dynamic and response surface methodology coupling: A new method for optimization of the duct to be used in ducted wind turbines*, Heliyon, 9(6), e17057.

WANG H K, LIU F Z, GAO J, et al., 2024. *Experimental analysis of coarse particle-wall collision and construction of a random rebound model,* The Ocean Engineering, 42(4), 96-109.

WANG J H, CHEN Q R, KUANG Y L, LYNCH, A.J., ZHUO J W, 2009. *Grinding process within vertical roller mills: experiment and simulation*, Mining Science and Technology, 19(01), 97-101.

WANG Z, JIA Y, LIU X, et al., 2022. *Removal of boron in desalinated seawater by magnetic metal-organic frame-based composite materials: Modeling and optimizing based on methodologies of response surface and artificial neural network,* Journal of Molecular Liquids, 349, 118090.

XU D, SHEN Y., 2024. *A novel CFD-DEM-DPM modelling of fluid-particles-fines reacting flows*, Chemical Engineering Science, 292, 120014.

XU Z G, LU S C, ZHANG Q, 2000. *Influence of blade spacing on the classification performance of a rotor-type ultra-fine classifier*, Mining and Metallurgical Engineering, (2), 25-27.